Absolute measurement of the relativistic magnetic dipole transition in He-like sulfur

Jorge Machado [1,*] Nancy Paul [2,†] Gabrielle Soum-Sidikov [2,3,‡] Louis Duval,[2,4] Stéphane Macé,[4] Robert Loetzsch,[5,6] Martino Trassinelli [4] and Paul Indelicato[2,§]

[1]*Laboratory of Instrumentation, Biomedical Engineering and Radiation Physics, Department of Physics,*
NOVA School of Science and Technology, NOVA University Lisbon, 2829-516 Caparica, Portugal
[2]*Laboratoire Kastler Brossel, Sorbonne Université, CNRS, ENS-PSL Research University, Collège de France,*
Case 74, 4, Place Jussieu, 75005 Paris, France
[3]*MINES ParisTech, Université PSL, 75006 Paris, France*
[4]*Institut des NanoSciences de Paris, CNRS, Sorbonne Université, 75005 Paris, France*
[5]*Helmholtz-Institut Jena, Fröbelstieg 3, 07743 Jena, Germany*
[6]*Institut für Optik und Quantenelektronik, Friedrich-Schiller-Universität Jena, Max-Wien-Platz 1, 07743 Jena, Germany*

We have made an absolute, reference-free measurement of the $1s2s\ ^3S_1 \rightarrow 1s^2\ ^1S_0$ relativistic magnetic dipole transition in He-like sulfur. The highly charged sulfur ions were provided by an electron-cyclotron resonance ion source, and the x rays were analyzed with a high-precision double-crystal spectrometer. A transition energy of 2430.3685(97) eV was obtained and is compared to most advanced bound-state quantum electrodynamics calculations, providing an important test of two-electron QED effects and precision atomic structure methods in medium-Z species. Thanks to the extremely narrow natural linewidth of this transition and to the large dispersion of the spectrometer at this energy, a complementary study is also performed to evaluate the impact of different silicon crystal atomic form-factor models in the transition-energy analysis. We find no significant dependence on the model used to determine the transition energy.

I. INTRODUCTION

Tests of bound-state quantum electrodynamics (BSQED) are pursued with precision measurements in complementary atomic systems, where the close comparison between experiment and theory allows us to disentangle the various facets of the theory. Highly charged ions (HCIs), i.e., few-electron atomic systems, are a privileged terrain of study as the quantum many-body problem can be solved most exactly for these systems, and their strong Coulomb fields lead to amplified BSQED effects in their atomic structure. Laser spectroscopy of normal and muonic hydrogen allows us to test perturbative BSQED to the threshold of third-order effects and to measure the charge radius of the proton [1–4], deuton [5], and the α particle [6]; see [7] for a recent review. High-precision measurements of transition energies, such as the work presented here, allow for precision tests of BSQED energy corrections such as self-energy and vacuum polarization or electron-electron and many-body relativistic effects; see [8] for a recent review. Precision measurements of other quantities, like Landé g factors in HCIs [9–11] and g factor

differences of coupled ions [12], also allow us to test BSQED contributions, to measure fundamental constants [13], and to place limits on new physics beyond the standard model.

H-like, single-electron systems have been studied across a broad range of species up to uranium, but far fewer measurements exist for He-like species [8]. A systematic divergence between experiment and BSQED theory for He-like systems has been observed [14,15], and an active ongoing discussion continues in the literature [8,16–21], which all points to the need for more high-precision data for He-like ions across a broad range of Z. This task is complicated due partly to the fact that, when moving beyond the lightest ions, the transition energies enter the x-ray regime, making direct laser spectroscopy impossible. While new approaches with coherent laser spectroscopy and quantum logic are promising [22,23], currently, the highest-precision method broadly applicable for determining transition energies in HCIs is using crystal spectrometers. These instruments may be coupled with electron-beam ion traps (EBITs), electron-cyclotron-resonance ion sources (ECRISs), and high-energy storage rings depending on the desired atomic number, charge state, and targeted transition [8]. With these methods, parts per million ($\Delta E/E \sim 10^{-6}$) accuracy can be achieved for medium-Z species, which allows us to probe two-electron QED effects. Here we present a measurement of the $1s2s\ ^3S_1 \rightarrow 1s^2\ ^1S_0$ relativistic magnetic dipole transition energy in He-like sulfur using a reflection double-crystal spectrometer (DCS). The use of such spectrometers has a long history. Our DCS, described in Ref. [24], is based on the design of the vacuum DCS of the

---

*jfd.machado@fct.unl.pt

†nancy.paul@lkb.upmc.fr

‡Present address: IRFU, CEA, Université Paris-Saclay, 91191 Gif-sur-Yvette, France.

§paul.indelicato@lkb.upmc.fr; http://www.lkb.upmc.fr/metrology simplesystems/project/paul-indelicato/.

National Institute of Standards and Technology (NIST) [25]. DCSs allow us to make measurements with accuracies around 1 ppm in an energy range close to the S and Ar $M1$ energy without any external reference to theoretical or experimental transition energies if the crystal lattice spacing is known accurately. For example, the broad L lines of Xe were measured at NIST [26] across an energy range from 3.6 to 4.2 keV with accuracies ranging from 20 to 40 meV. Recent work at NIST provides a detailed study of the systematics involved and uses techniques similar to those employed in the present work [27]. The S $M1$ measurement provided here is compared to the most advanced BSQED calculations. The theoretical S and Ar $M1$ lines have also been used as standards to measure other HCI lines in S and Ar [28] with a spherically curved crystal. The present work and Ref. [17] allow us to improve the significance of comparison to theory of such measurements since fully experimental values can then be deduced.

II. EXPERIMENTAL METHOD

The measurements were performed at the Laboratoire Kastler Brossel in Paris using the unique experimental setup that couples a high-intensity ECRIS with a DCS [24,29]. The ECRIS, called SIMPA (Source d'Ions Multichargés de Paris), is jointly operated by the Laboratoire Kastler Brossel and the Institute des Nanosciences de Paris on the Pierre and Marie Curie campus of Sorbonne University. SIMPA uses 14.5-GHz microwaves to create an intense plasma of highly charged ions of medium-Z gaseous species, with a source size of a few centimeters, making it well adapted to crystal spectrometers. The electron temperature inside the ECRIS can reach 46 keV for light elements like Ar [30], allowing us to create core-excited He-like ions. The trapping depth in the source has been determined based on an analysis of Doppler broadening and comparison with simulations to be ≈ 0.2 V [30], meaning that the ions have kinetic energies smaller than ≈ 0.2 eV $\times q$, where q is the ion charge. This leads to Doppler broadening of the emitted transitions of approximately 100 meV [17]. It should be noted that in precision measurements using EBITs [16,18], the depth of the trapping potential is around 200 V, which leads to a larger broadening. Furthermore, the relative intensities of the observed lines produced by an ECRIS differ from those in an EBIT. While the strongest line observed in an EBIT is the $1s2p\ ^1P_1 \rightarrow 1s^2\ ^1S_0$ diagram line, it is the relativistic $M1$ that is the strongest line observed in an ECRIS. The diagram line has also been measured in argon [21] but is less intense than $M1$. This is due to the different processes that populate the initial level in the two sources. While the $1s2s\ ^3S_1$ level is mostly created by ionization through the electron impact of the Li-like sulfur ground state $1s^22s\ ^2S_{1/2}$, the $1s2p\ ^1P_1$ level is populated by excitation of the $1s^2\ ^1S_0$ ground state of the He-like sulfur, which is much less abundant in the ECRIS plasma, thus leading to a less intense line compared to $M1$.

The DCS uses two 6×4 cm^2, 6-mm-thick Si(111) crystals made by NIST, whose lattice spacing in vacuum has been measured to a relative uncertainty of 0.012×10^{-6} [24] at a temperature of 22.5 °C with respect to the definition of the meter. The DCS is thus a reference-free instrument, as the measured wavelengths are directly connected to the

definition of the meter. The DCS operates in reflection mode and is capable of attaining world-record precision of a few parts per million ($\Delta E/E \sim 10^{-6}$) for few-keV x rays emitted by highly charged ions. The optical axis of the spectrometer is aligned with the source axis so that the DCS can see x rays emanating directly from the plasma. A detailed description of the experimental setup may be found in [17,21,24].

The experimental campaign was conducted in 2018 and focused on the $1s2s\ ^3S_1 \rightarrow 1s^2\ ^1S_0$ magnetic dipole $M1$ transition in He-like sulfur. This same transition was measured in Ar during a previous data-taking period [17], but as the sulfur transition is located at lower energy, the dispersion in the instrument is higher, and here we are thus able to perform a more sensitive measurement. These $M1$ transitions are unique as they have a natural linewidth that is negligible with respect to the broadening induced by the crystal response of the DCS. Thus, after accounting for the small Gaussian Doppler broadening due to the temperature of the ions trapped in the space charge of the electrons, which has been well characterized [17,24,30], the line shape that we obtain for these transitions is directly related to the spectral response of the photons diffracting through the crystal structure. The fundamental description of this phenomenon is provided by dynamical diffraction theory and atomic form factors, the latter of which describes the response of the electronic cloud of the Si atoms in the crystal to the incident radiation.

The measurement and analysis principles were described in detail elsewhere [24], and here only the key points will be summarized. During a measurement, the first crystal is maintained at a fixed position and acts as a first selector in energy as only a small range of photon energies will be reflected onto the second crystal. The second crystal is then oriented in one of two modes: (1) nondispersive, where the two crystals are parallel and the outgoing x-ray beam is parallel to the incoming beam, or (2) dispersive, where the two crystals deflect the x rays in the same direction. The peak shape obtained when the two crystals are parallel, i.e., in the nondispersive mode, depends only on the experimental geometry and reflection profile of the crystals. In the dispersive mode the peak shape is a convolution of the instrument response function and of the line shape of the transition. The angular difference between the two modes of the second crystal can be directly connected to the Bragg angle, thus allowing one to analyze the energy of the x rays. A microstepping motor rotates the second crystal continuously within a predefined range for each mode, and the number of x rays is recorded along with the crystal angles and temperatures. During a typical day of measurement, the majority of the time is spent measuring the dispersive-mode spectrum, and nondispersive-mode spectra are taken at the beginning and end of the day for a given transition. An example of dispersive- and nondispersive-mode spectra for the $M1$ transition in He-like sulfur is shown in Fig. 1.

The analysis of the data is based on an *ab initio* simulation of our spectrometer [24], which performs exact ray tracing based on the geometry of our setup and of the ECRIS source. The simulation uses as input the reflectivity profiles (commonly called "rocking curves") for the Si(111) crystals obtained from an x-ray tracing program based on dynamical
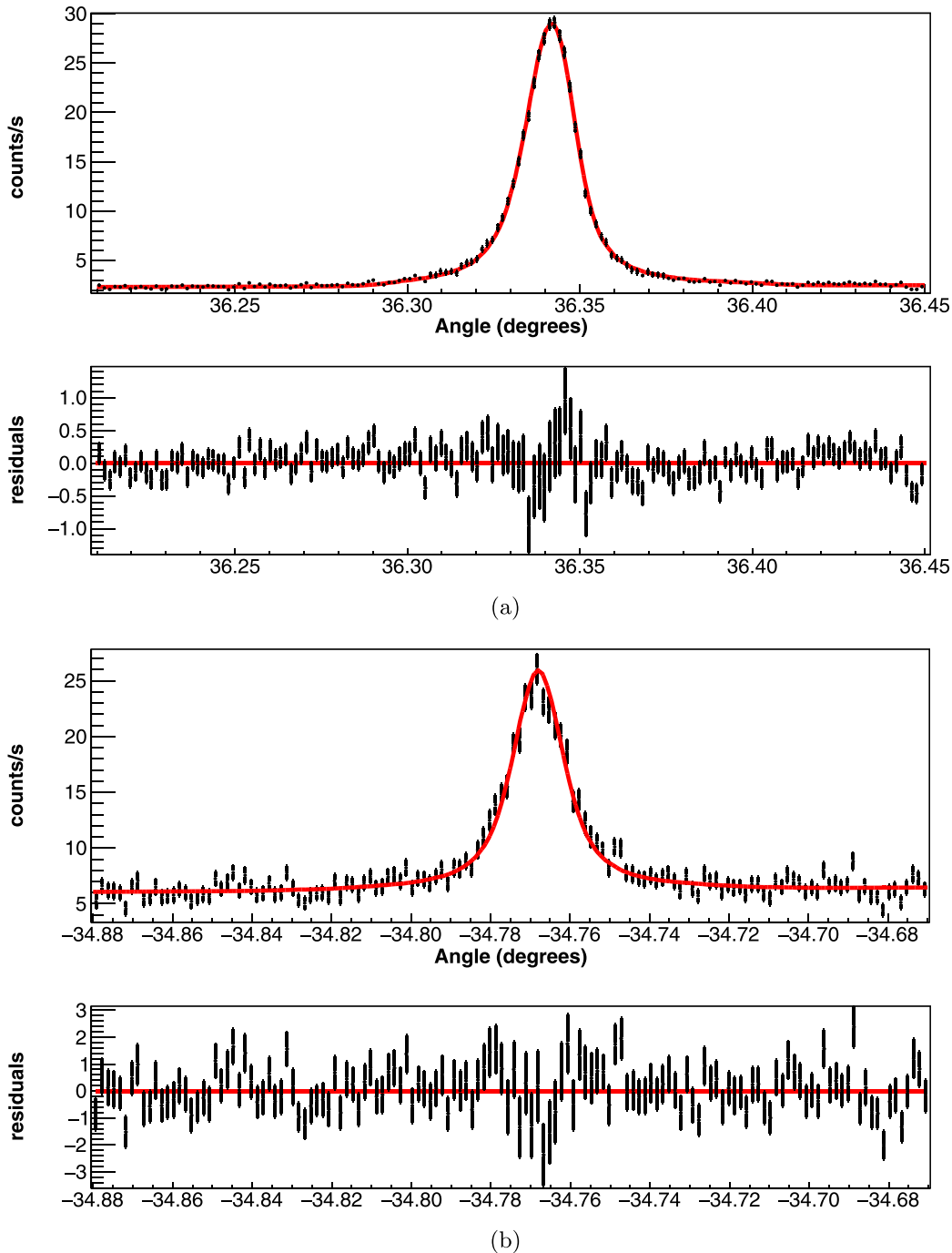
FIG. 1. Experimental pair of dispersive and nondispersive (parallel) spectra for the $1s2s\ ^3S_1 \rightarrow 1s^2\ ^1S_0$ transition in He-like sulfur. (a) Top: Experimental dispersive spectrum for the $1s2s\ ^3S_1 \rightarrow 1s^2\ ^1S_0$ transition in He-like sulfur (black points) with 68 993 integrated counts, fit with a simulated response function and linear background (red curve) with a corresponding reduced χ^2 of 1.38. Bottom: The fit residuals. (b) Top: Experimental nondispersive (parallel) spectrum for the $1s2s\ ^3S_1 \rightarrow 1s^2\ ^1S_0$ transition in He-like sulfur (black points) with 15 205 integrated counts, fit with a simulated response function and linear background (red curve) with a corresponding reduced χ^2 of 1.36. Bottom: The fit residuals.

diffraction theory. The rocking curves used in the analysis presented here were obtained using the x-ray oriented program (XOP) [31–33]. The response functions obtained from this simulation are then used to fit the experimental spectra and determine the transition energies and widths of the measured transitions.

A. Evaluation of the Doppler widths

In the analysis procedure described in detail in [17,21,24,34], we must first determine the Doppler broadening of the lines. For the forbidden transition considered here, this is straightforward as the natural width of the line is negligible, so all the broadening seen in the spectra that
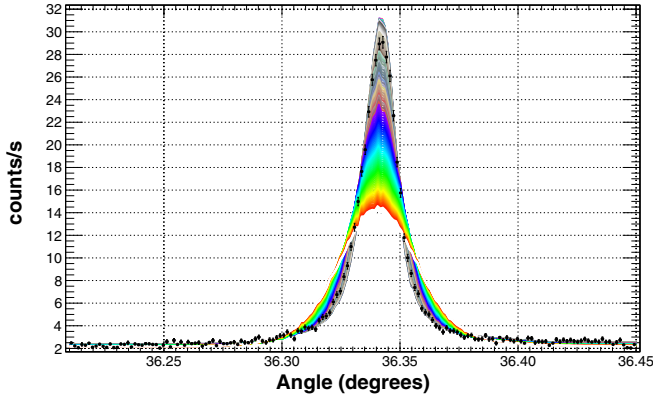
FIG. 2. Experimental dispersive spectra fit with simulated response functions with different Gaussian Doppler widths, from 0 to 500 meV. The colors from black to red indicate minimal and maximal simulated Doppler widths, respectively.

cannot be explained by the spectrometer response function is due to the Doppler effect. Using the *ab initio* simulation of our setup, first, a set of response functions is simulated for the dispersive spectra with different Doppler widths Γ_G^i ranging from 0 to 500 meV, assuming the theoretical line energy, setting the temperature in the simulation to $T = 22.5\,^\circ\text{C}$, and setting the Lorentzian (natural) linewidth to zero. The dispersive spectra are then fitted with these simulations superimposed on a linear background using the function

$$I(\theta - \theta_0, I_{\max}, a, b) = I_{\max} S_{E_0, \Gamma_G^i, T_0}(\theta - \theta_0) + b\theta + a, \quad (1)$$

where $S_{E_0, \Gamma_G^i, T}$ is the set of simulated response functions with different Gaussian widths, line energy E_0, and temperature T. The fitting parameters are the peak intensity $I_{\max}$, the peak centroid θ, and the background slope b and offset a. An example fit is shown in Fig. 1(a).

The quality of the fit is then evaluated by considering the evolution of χ^2 as a function of Gaussian width. Each experimental dispersive spectrum is fitted with the set of simulations with different Γ_G^i, and the minimum in the χ^2 curve is determined for each spectrum. Figure 2 shows an example of the fits to a dispersive-mode spectrum with a set of response functions with Gaussian widths in the 0- to 500-meV range. The χ^2 trend is shown in Fig. 3 for the different fits of a single sulfur spectrum. The trend was fitted with an eighth-degree polynomial to obtain the minimum. This analysis was also checked by using the NESTEDFIT [35] Bayesian analysis fitting program based on the methods described in [36]. In this approach, the log of the Bayesian evidence of each fit to the dispersive spectrum is evaluated as a function of the simulated Doppler width, and the maximum of the evidence generally indicates the maximum likelihood. The Bayesian evidence, also called marginalized likelihood, is obtained by the integration of the likelihood function over the fit parameters. The (logarithmic) values of the evidence as a function of the Doppler width were then evaluated and fitted with both an eighth-degree polynomial and splines. The weighted average of the maximum obtained with both polynomial and spline regressions was taken to determine the Doppler broadening from each spectrum. The standard uncertainty with this
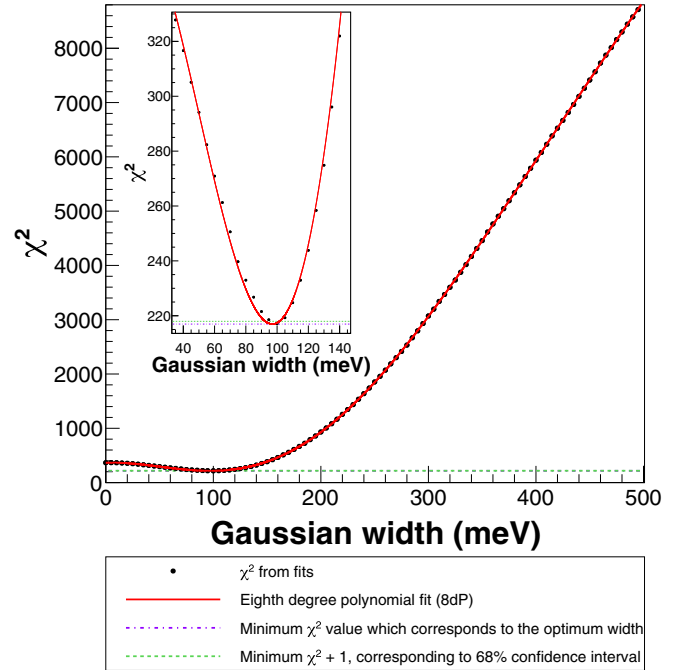

FIG. 3. χ^2 of the fit to the dispersive spectrum as a function of Gaussian width (black points). The trend has been fitted with an eighth-degree polynomial (red line).

method is given by a ln(evidence) offset of 0.96 from the maximum evidence, which corresponds to the 2σ confidence range, the accepted standard for Bayesian evidence analysis uncertainty extraction [37]. The evolution of the Doppler broadening obtained in this way for the different sulfur spectra is shown in Fig. 4. The small fluctuations correspond to daily variations in the ECRIS source parameters.

A weighted average of all the sulfur spectral widths was evaluated to obtain an average Doppler broadening of 0.093(7) eV (FWHM), in agreement with the results of the χ^2 minimization of 0.095(7) eV. This Doppler width was then used for the transition-energy analysis described below. Note that this Doppler width is slightly larger than the value published following our analysis of transitions in Li-like sulfur [34], in which a value of 0.0917(74) eV was
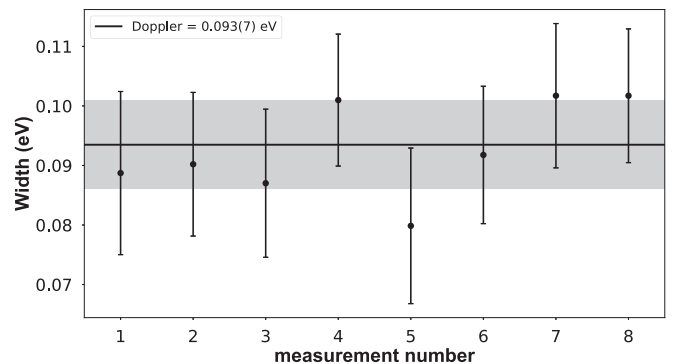

FIG. 4. Doppler width as extracted from each dispersive spectrum with the statistical error bars. The weighted average and its uncertainty are shown as the solid line and shaded bar, respectively.

obtained, although they agree within their statistical uncertainties. We checked the impact of this small change and found that performing the analysis with the Doppler width fixed at 0.0950 eV, instead of 0.0917 eV, leads to changes in the natural linewidths of the $1s2s2p\,^2P_{1/2,3/2} \rightarrow 1s^2 2s\,^2S_{1/2}$ transitions of 0.3% and 0.8%, respectively, which are negligible with respect to the 17.5% and 24.4% uncertainties on these linewidths.

B. Evaluation of transition energies

With the Doppler broadening determined from the analysis described above, a new set of simulations for both nondispersive and dispersive modes is performed for different transition energies E_i and crystal temperatures T_l, which both shift the line position. The energies are simulated in a grid around the theoretical transition energy according to $E_i = E_{\text{theo}} + i\Delta E$, where ΔE is an energy step (generally, $\approx$10 meV) and i is an integer that can take positive or negative values. Each E_i is simulated for different crystal temperatures $20\,^\circ\text{C} \leqslant T \leqslant 25\,^\circ\text{C}$. Each experimental spectrum is then fitted according to Eq. (1), where now $E_0 = E_i$, $T_0 = T_l$, and the Gaussian broadening Γ_G^i is fixed to the value obtained with the procedure described in Sec. II A.

For each experimental pair of dispersive and nondispersive spectra, corresponding to a day of measurement, the offsets in angle between the simulated and experimental spectra are determined, where the offsets are given by

$$\Delta\theta_{\text{Exp-Sim}}^{n,k,l} = \left(\theta_{\text{Exp-D}}^n - \theta_{\text{Exp-ND}}^n\right) \\ - \left(\theta_{\text{Sim-D}}^{k,l} - \theta_{\text{Sim-ND}}^{k,l}\right). \quad (2)$$

In the above expression, n indicates a given pair of dispersive (D) and nondispersive (ND) spectra, resulting from a single day of measurement. If $\Delta\theta_{\text{Exp-Sim}}^{n,k,l} = 0$, the temperature and energy of the simulation correspond to those of the experiment. The angular offset $\Delta\theta_{\text{Exp-Sim}}^{n,k,l}$ is then evaluated on the grid of simulated energies and temperatures and fitted with the bidimensional function:

$$\Delta\theta_{\text{Exp-Sim}}(E, T) = p + qE + rE^2 + sET + uT + vT^2. \quad (3)$$

For each pair of experimental spectra n, the above expression is used to obtain the experimental line energy by determining where $\Delta\theta_{\text{Exp-Sim}}(E_{\text{exp}}^n, T_{\text{exp}}) = 0$, where T_{exp} is the measured temperature of the second crystal. An example of an angular offset surface used to obtain the transition energy from a pair of measurement spectra is shown in Fig. 5. The transition energies extracted from each pair of spectra are then averaged to obtain the final transition energy, including statistical uncertainties of 2430.3685(53) eV, as shown in Fig. 6.

Table I shows the experimental systematic uncertainties and their contributions (in eV) to the uncertainties on the transition energies. Including these effects, the final transition energy is 2430.3685(97) eV. Note that with respect to our previous works [24,34], the systematic uncertainty associated with the energy-to-wavelength conversion has been removed since the new definition of the International System of Units in 2018 defined the Planck constant to be exact [38], as the speed of light has been since 1983. Nevertheless, this redefinition has a negligible effect on our systematic uncertainty. As the
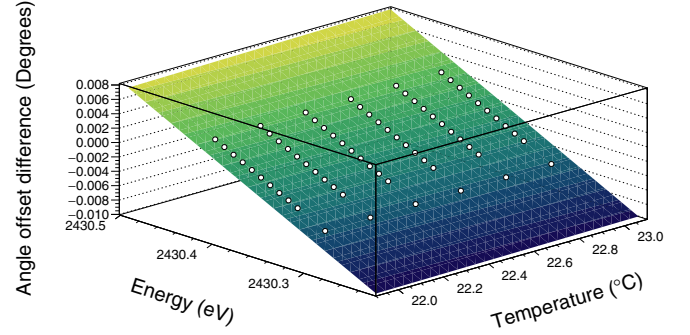

FIG. 5. Fitted two-dimensional angular offset function from Eq. (2) and experimental results (white spheres) for an example pair of experimental spectra for the sulfur $M1$ transitions. The fit is performed while taking into account the statistical error bars for each point.

energy of the sulfur $M1$ transition is lower than the one in Ar, the Bragg angle increases from 39.56° to 54.44°. This leads to increased dispersion, and thus, the angular encoder error effect is reduced from 0.0036 eV in Ar to 0.00171 eV in S. For the same reason, the effect of the temperature stabilization contribution to the uncertainty is decreased.

However, other contributions due to crystal structure are increased due to the higher sensitivity to the shape of the simulated spectra. The contributions associated with the crystal structure and geometric effects are evaluated through simulations, following the procedure described in Ref. [24]. All geometric effects (crystal tilts, vertical divergence, and variation of x-ray source size) yield a higher-energy shift in S than in Ar. This means that for higher dispersion there is an increase in sensitivity to possible misalignments of the instrument and to the unknown spatial location of the ions in the plasma. Thus, these effects have a higher impact on the final uncertainty for larger Bragg angles. For instance, the
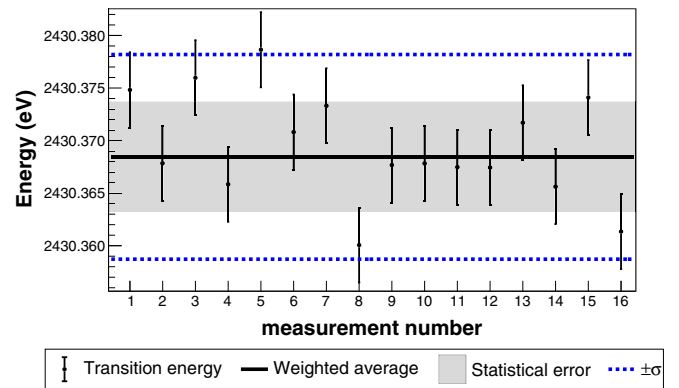

FIG. 6. Results of the transition-energy analysis for the different pairs of dispersive and nondispersive spectra recorded during the experiment. The error bars on the points correspond to the statistical, temperature, and angle-encoder measure uncertainties added in quadrature. The black solid line represents the weighted average considering only the statistical uncertainty of each point. The gray shaded region corresponds to the weighted standard deviation. The blue dashed lines indicate the standard uncertainty on the weighted average including both statistical and systematic uncertainties.

TABLE I. Contributions to the systematic uncertainties for the *M*1 transition in sulfur. All energies are given in eV.

Contribution	Value
Angular encoder error (0.2″)	0.00171
Temperature stabilization (0.5 °C)	0.00312
Vertical tilts of crystals (±0.01°) for each crystal	0.00085
Vertical divergence (1 mm)	0.00102
Variation of x-ray source size from 6 mm to 12 mm	0.00462
Si crystal atomic form factor	0.00300
X-ray polarization	0.00513
Lattice spacing error	0.00010
Index of refraction	0.00055
Thermal expansion	0.00015
Energy dependence of the Doppler width	0.00031
Total	0.00819

TABLE II. Comparison between experimental transition energy and theoretical values (eV). Calculated contributions to the $1s^2$ $^1S_0$ and $1s2s$ $^3S_1$ levels are from Ref. [40]. Uncertainties on the transition energies are indicated in parentheses.

Contribution	$1s^2$ $^1S_0$	$1s2s$ $^3S_1$	Transition
ΔE_{Dirac}	−3495.0044	−874.5000	2620.5044
ΔE_{int}	270.4822	80.9665	−189.5157
$\Delta E_{\text{1 el}}^{\text{QED}}$	0.7562	0.1014	−0.6548
$\Delta E_{\text{2 el}}^{\text{QED}}$	−0.0715	−0.0110	0.0605
$\Delta E_{\text{h.o.}}^{\text{QED}}$	0.0009	0.0002	−0.0007
ΔE_{rec}	0.0563	0.0137	−0.0426
Theory [40]	−3223.7803	−793.4292	2430.3511 (3)
Theory [41]			2430.35208 (89)
Expt. (this work)			2430.3685 (97)

position and location of HCIs in the plasma may change due to different conditions of the ECRIS operation, such as gas pressure and microwave power. In order to account for this source of uncertainty, the difference in energy obtained by the data-analysis procedure described in Sec. II B for two sets of simulations is considered: one for an x-ray source 12 mm in diameter, which corresponds to the diameter of the input collimator, and another source with a 6-mm diameter. The difference in energy resulting from these two simulations has been considered a largely overestimated contribution to the final error bar. While this effect has an impact of 1.30 meV in argon [17,24], for sulfur this energy difference is 4.62 meV. Due to this increase in sensitivity to the spectrum shape, the uncertainties related to crystal structure are also larger for S than for Ar. The simulated spectra considering different Si crystal form-factor databases are more disparate at this lower energy, thus yielding higher deviations in energy depending on which one is used. We thus use the difference in the results obtained with the three different form-factor databases as the uncertainty for this effect. A detailed investigation of the effect of form factors is presented in Sec. IV. A similar procedure is followed for the uncertainty coming from a possible polarization of the x rays. This effect is estimated by considering two different sets of simulations, one with an unpolarized reflectivity profile and another obtained with a σ-polarized reflectivity profile. The difference in transition energy obtained via the analysis using the different sets of simulations is considered to be the uncertainty due to the presence of any polarized x rays.

We have also added another source of uncertainty in the analysis of the energy of this line. As mentioned above, the Doppler broadening is evaluated as a weighted-average value of the one obtained for each individual dispersive spectrum. Therefore, we checked for a possible energy dependence in the analysis due to the Doppler width value used in the simulations. For the evaluation of this effect, we performed the data analysis with simulations with the average value for the Doppler width and with simulations with the average values $+\sigma$ and $-\sigma$. The largest energy deviation from the analysis considering the average value of the Doppler broadening is added to the uncertainty budget. Because of the contribution

of these effects, the final relative uncertainty is increased from 2.5 ppm in Ar to 4 ppm in S.

III. COMPARISON WITH THEORY

Our experimental transition energy compared with most advanced BSQED calculations is shown in Table II. Our result is particularly interesting to compare with theory, as this intermediate-*Z* region is at the interface where both perturbative methods with respect to the $Z\alpha$ parameter, best adapted for light-*Z* ions, and nonperturbative methods, best adapted for high-*Z* species, may be used but each is at the limit of its domain of applicability. It is also in this region that unaccounted for contributions from each of these methods may reach their maximum (see discussion in [39]); thus, precision experiments able to test these methods are essential. The theoretical results from Artemyev *et al.* [40] include the complete set of two-electron QED corrections of orders α and α^2 evaluated to all orders in *Z*, a method well adapted to high-*Z* species, whose accuracy is tested here for this medium-*Z* ion. The very recent calculations from Yerokhin *et al.* [41], building on their previous results [39], are based on the unified approach of Drake [42], which aims at bridging the gap between perturbative and nonperturbative calculations for medium-*Z* species, now with improvements to account for higher-order QED effects of order $m\alpha^{7+}$. Both calculations yield transition energies for this $1s2s$ $^3S_1 \rightarrow 1s^2$ $^1S_0$ line that are lower than our experimental result, 1.8σ and 1.7σ for [40,41], respectively. This same trend was observed when our group measured this same transition in He-like argon [17]. A comparison between existing experiments for the *M*1 transitions for $16 \leqslant Z \leqslant 29$ and recent calculations are presented in Fig. 7. A comparison of the theoretical values from Artemyev *et al.* [40,41] is also presented.

IV. SENSITIVITY TO ATOMIC FORM FACTORS

The *M*1 line studied in this work has a negligible natural linewidth; thus, it is a good probe to explore the systematic effects in our experiment linked to the experimental response function. Together with the Gaussian Doppler broadening as described in Sec. II A, the remaining line shape results
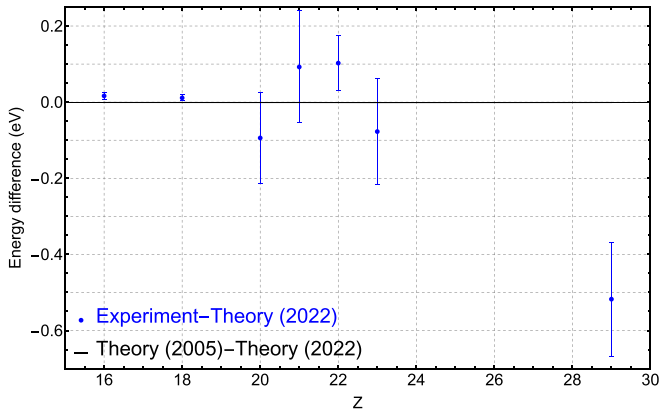
FIG. 7. Comparison between experiment and theory for the $1s2s\ ^3S_1 \to 1s^2\ ^1S_0$. $Z = 16$: this work, $Z = 18$: [17], $Z = 20$: [43], $Z = 21$: [44], $Z = 22$: [45], $Z = 23$: [46], $Z = 29$: [20]. Theory (2005): [40], Theory (2022): [41].

from the details of the interaction between the x rays and the Si(111) crystals within our experimental geometry. The interaction with each crystal must be described by dynamical diffraction theory (see, e.g., [47]), which takes into account penetration of the x rays in the crystal and multiple scattering. The differential absorption in the crystal must also be taken into account. This is included in the simulation programs we use and leads to the shift between the Bragg angle and the real position of the diffraction peak, as shown in Fig. 8, and to the slight line asymmetry.

For a photon scattering elastically on an atom (in this case the Si atoms), the scattering process can be broken up into three different processes: nuclear Thomson and nuclear resonance scattering; bound electron scattering, also known as Rayleigh scattering; and Delbruck scattering, which accounts for vacuum fluctuations in the Coulomb field of the nucleus. As nuclear and vacuum fluctuation effects become significant only at high energies and large angles, the contributions that play a role in our case are photoabsorption and forward-angle Rayleigh scattering [48,49].

For ease of use, resonant scattering amplitudes are generally described using atomic form factors (FFs) [50]. The FF is the Fourier transform of the electron distribution of the atom and is generally written as the sum of three terms: an angle-dependent term f_0 and two angle-independent terms, f_1 and f_2, which account for energy-dependent reflection and absorption, respectively. f_1 and f_2 are known as anomalous scattering factors and may also be expressed as f' and f'' depending on the notation, which can be related to f_1 and f_2 via a constant factor. The available FF databases are based on experimental data, S-matrix theory, or some combination of the two. Average discrepancies between different theories are 10%–30% but may be much larger near absorption edges. Below a few keV, in the region of interest here, the available data to constrain FFs from photoabsorption measurements have large experimental uncertainties and are thus unable to discriminate between different FF models [51], hence the interest in testing the FF sensitivity in this measurement. In a more recent work, the mass absorption coefficient of silicon was measured with improved accuracy [52], and the difference
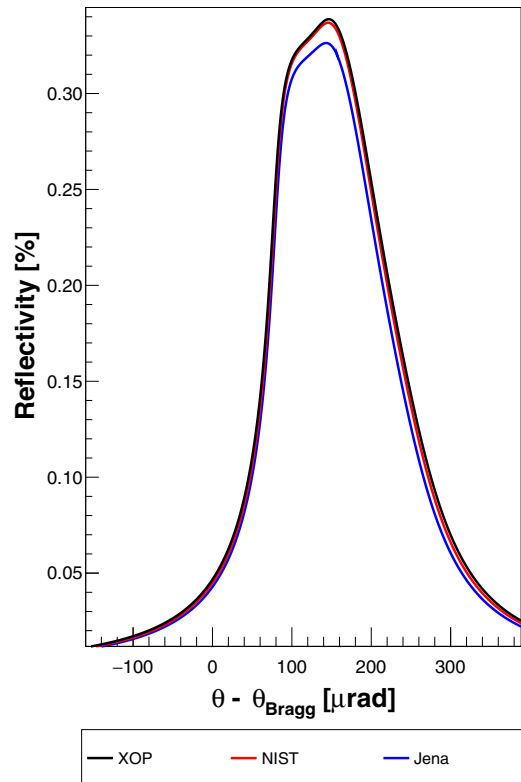

FIG. 8. Si(111) rocking curves for unpolarized radiation $\frac{1}{2}(\pi$ polarized $+ \sigma$ polarized) calculated with the different models used to produce the DCS response functions. The curves have been evaluated for the theoretical energy of the $1s2s\ ^3S_1 \to 1s^2\ ^1S_0$ transition of 2430.3511 eV taken from Ref. [40].

between these measurements and tabulated and theoretical values is of the order of a few percent.

Sensitivity to the FF was tested by generating experimental response functions using rocking curves obtained from the Jena, XOP-Henke, and NIST codes. NIST refers to the MCX-TRACE program [53] that uses the RTAB form-factor database [54] from S-matrix calculations for the $f1$ and $f2$ components and the NIST FFAST database for f_0 [49,51]. XOP uses the Henke database [50]. The Jena model, DIXI [55], uses the Henke experimental database and theoretical values from Sasaki [56]. Si(111) rocking curves from these three models for the x-ray energy regime of interest are shown in Fig. 8. As explained previously, these rocking curves are used as inputs for our *ab initio* simulation of our spectrometer used to generate the simulated instrumental response functions.

The data analysis was then performed as described in Secs. II A and II B. Doppler broadenings were simulated in the range from 0 to 116 meV FWHM. The experimental dispersive spectra were fitted with these simulated spectra using the Bayesian analysis toolkit NESTEDFIT [35]. For each experimental spectrum and FF model, the Bayesian evidence was obtained as a function of the Doppler width, the results were fit with an eighth-order polynomial, and the evidence maximum and change in ln(evidence) of 0.96 were used to determine the Doppler broadening and associated uncertainty for each spectrum. The results for a single dispersive spectrum are shown in Fig. 9, where it is clear that the maximum shifts
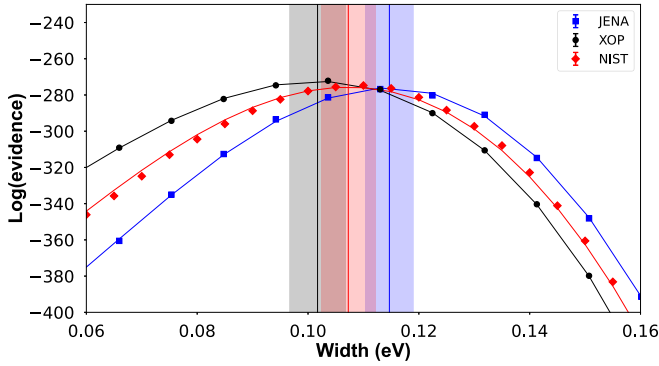
FIG. 9. Bayesian evidence (BE) curves for different Doppler widths for a single experimental dispersive spectrum. Fits are shown with response functions generated with different atomic form-factor models. The BE uncertainties are smaller than the size of the points. The BE trends as a function of width are shown fit with eighth-degree polynomials, from which the maximum evidence and standard BE uncertainty are obtained, shown by the solid lines and colored bars, respectively.

slightly for the different FF models. XOP and NIST models yield Doppler widths consistent within the uncertainties, but the results from the Jena model are not compatible with XOP, and the Jena model yields a larger Doppler width. This may be understood by examining the line shapes in Fig. 8, where it is clear that the rocking curve obtained with the Jena model is narrower than the others.

Using these Doppler widths, the energy analysis was then performed following the procedure in Sec. II B. The results with the averages over the different pairs of experimental
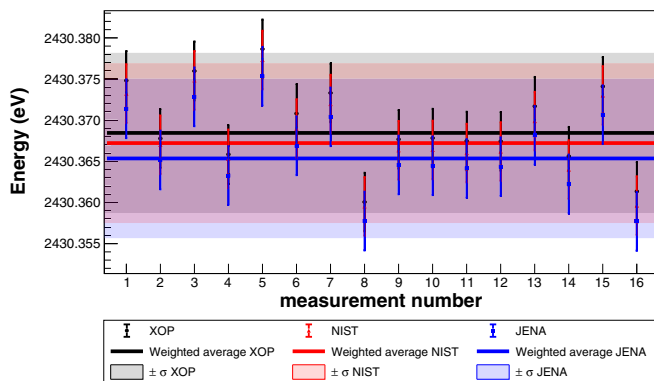

FIG. 10. Comparison of the transition-energy results from analyses using different models for the reflective-profile calculation. The error bars on the points correspond to the statistical, temperature, and angle-encoder measure uncertainties added in quadrature. The black dots correspond to the energy values extracted in the analysis using simulations performed with XOP [31–33] calculated profiles, the red triangles are from those using NIST profiles [53], and the blue squares correspond to those using JENA [55] profiles. The black, red, and blue solid lines represent the weighted averages of the different energy values using the respective points of same color. In the weighted-average calculation of the energy for each model, only the statistical uncertainty of each point is considered. The shaded areas correspond to the statistical uncertainty.

TABLE III. Comparison of Doppler widths and transition energies determined using different atomic form-factor models. All energies are given in eV.

Model	Observable	Value
XOP	Doppler width	0.093(7)
NIST	Doppler width	0.100(7)
Jena	Doppler width	0.108(6)
XOP	Energy	2430.3685(97)
NIST	Energy	2430.3672(97)
Jena	Energy	2430.3654(97)

spectra are shown in Fig. 10. Unlike the evaluation of the Doppler widths, the average transition energies extracted with the different FF models are compatible within the statistical uncertainties. This shows that these FFs cannot be a significant source of uncertainty in the comparison with the BSQED calculations, confirming the systematic uncertainty related to the FFs included in Table I.

We note that there is a statistically significant difference in the absolute value of the Bayesian evidence for the different FF models; that is, it is possible to determine which line shape corresponds most closely with our data, but a full study of this effect is beyond the scope of this analysis. A summary of the Doppler widths and transition energies obtained with the different FF models is given in Table III.

V. CONCLUSION

We have measured the $1s2s\ {}^3S_1 \rightarrow 1s^2\ {}^1S_0$ transition in He-like sulfur. The measurement was performed using the Paris double-crystal spectrometer and is thus reference free. The measured transition energy is 2430.3685(97) eV, which is in agreement with the most advanced QED calculations within 2σ. With an accuracy of 4 ppm, this is the second most accurate measurement of the He-like $M1$ transition energy after the one we performed in Ar with a relative accuracy of 2.5 ppm. The extremely narrow natural linewidth of the transition allowed us to perform a complementary study of the effect of the choice of the Si crystal atomic form-factor model in our experimental response functions, as we use them here for an analysis in a region that is poorly constrained experimentally. We found that although the different models yield different Doppler broadenings, this does not have a significant impact on our transition-energy analysis. Further work will aim at extending our analysis of He-like ions to higher-Z species, complementing ongoing studies of He-like uranium at the GSI Helmholtzzentrum für Schwerionenforschung facility.

ACKNOWLEDGMENTS

[1] A. D. Brandt, S. F. Cooper, C. Rasor, Z. Burkley, A. Matveev, and D. C. Yost, Phys. Rev. Lett. **128**, 023001 (2022).

[2] A. Grinin, A. Matveev, D. C. Yost, L. Maisenbacher, V. Wirthl, R. Pohl, T. W. Hänsch, and T. Udem, Science **370**, 1061 (2020).

[3] N. Bezginov, T. Valdez, M. Horbatsch, A. Marsman, A. C. Vutha, and E. A. Hessels, Science **365**, 1007 (2019).

[4] H. Fleurbaey, S. Galtier, S. Thomas, M. Bonnaud, L. Julien, F. Biraben, F. Nez, M. Abgrall, and J. Guéna, Phys. Rev. Lett. **120**, 183001 (2018).

[5] R. Pohl, F. Nez, L. M. P. Fernandes, F. D. Amaro, F. Biraben, J. M. R. Cardoso, D. S. Covita, A. Dax, S. Dhawan, M. Diepold *et al.*, Science **353**, 669 (2016).

[6] J. J. Krauth, K. Schuhmann, M. A. Ahmed, F. D. Amaro, P. Amaro, F. Biraben, T.-L. Chen, D. S. Covita, A. J. Dax, M. Diepold *et al.*, Nature (London) **589**, 527 (2021).

[7] J.-P. Karr, D. Marchand, and E. Voutier, Nat. Rev. Phys. **2**, 601 (2020).

[8] P. Indelicato, J. Phys. B **52**, 232001 (2019).

[9] J. Verdú, S. Djekić, S. Stahl, T. Valenzuela, M. Vogel, G. Werth, T. Beier, H.-J. Kluge, and W. Quint, Phys. Rev. Lett. **92**, 093002 (2004).

[10] S. Sturm, A. Wagner, M. Kretzschmar, W. Quint, G. Werth, and K. Blaum, Phys. Rev. A **87**, 030501(R) (2013).

[11] A. Wagner, S. Sturm, F. Köhler, D. A. Glazov, A. V. Volotka, G. Plunien, W. Quint, G. Werth, V. M. Shabaev, and K. Blaum, Phys. Rev. Lett. **110**, 033003 (2013).

[12] T. Sailer, V. Debierre, Z. Harman, F. Heiße, C. König, J. Morgner, B. Tu, A. V. Volotka, C. H. Keitel, K. Blaum *et al.*, Nature (London) **606**, 479 (2022).

[13] J. Zatorski, B. Sikora, S. G. Karshenboim, S. Sturm, F. Köhler-Langes, K. Blaum, C. H. Keitel, and Z. Harman, Phys. Rev. A **96**, 012502 (2017).

[14] C. T. Chantler, M. N. Kinnane, J. D. Gillaspy, L. T. Hudson, A. T. Payne, L. F. Smale, A. Henins, J. M. Pomeroy, J. N. Tan, J. A. Kimpton, E. Takacs, and K. Makonyi, Phys. Rev. Lett. **109**, 153001 (2012).

[15] C. T. Chantler, A. T. Payne, J. D. Gillaspy, L. T. Hudson, L. F. Smale, A. Henins, J. A. Kimpton, and E. Takács, New J. Phys. **16**, 123037 (2014).

[16] H. Bruhns, J. Braun, K. Kubiček, J. R. Crespo López-Urrutia, and J. Ullrich, Phys. Rev. Lett. **99**, 113001 (2007).

[17] P. Amaro, S. Schlesser, M. Guerra, E. O. Le Bigot, J.-M. Isac, P. Travers, J. P. Santos, C. I. Szabo, A. Gumberidze, and P. Indelicato, Phys. Rev. Lett. **109**, 043005 (2012).

[18] K. Kubiçek, P. H. Mokler, V. Mäckel, J. Ullrich, and J. R. Crespo López-Urrutia, Phys. Rev. A **90**, 032508 (2014).

[19] S. W. Epp, R. Steinbrügge, S. Bernitt, J. K. Rudolph, C. Beilmann, H. Bekker, A. Müller, O. O. Versolato, H. C. Wille, H. Yavaş, J. Ullrich, and J. R. Crespo López-Urrutia, Phys. Rev. A **92**, 020502(R) (2015).

[20] P. Beiersdorfer and G. V. Brown, Phys. Rev. A **91**, 032514 (2015).

[21] J. Machado, C. I. Szabo, J. P. Santos, P. Amaro, M. Guerra, A. Gumberidze, G. Bian, J. M. Isac, and P. Indelicato, Phys. Rev. A **97**, 032517 (2018).

[22] P. Micke, T. Leopold, S. A. King, E. Benkler, L. J. Spieß, L. Schmöger, M. Schwarz, J. R. C. López-Urrutia, and P. O. Schmidt, Nature (London) **578**, 60 (2020).

[23] S. A. King, L. J. Spieß, P. Micke, A. Wilzewski, T. Leopold, E. Benkler, R. Lange, N. Huntemann, A. Surzhykov, V. A. Yerokhin *et al.*, Nature (London) **611**, 43 (2022).

[24] P. Amaro, C. I. Szabo, S. Schlesser, A. Gumberidze, E. G. Kessler, A. Henins, E. O. Le Bigot, M. Trassinelli, J. M. Isac, P. Travers *et al.*, Radiat. Phys. Chem. **98**, 132 (2014).

[25] R. D. Deslattes, Rev. Sci. Instrum. **38**, 815 (1967).

[26] T. Mooney, E. Lindroth, P. Indelicato, E. G. Kessler, Jr., and R. D. Deslattes, Phys. Rev. A **45**, 1531 (1992).

[27] C. I. Szabo, J. P. Cline, A. Henins, L. T. Hudson, and M. H. Mendenhall, J. Res. Natl. Inst. Stand. Technol. **126**, 126049 (2021).

[28] S. Schlesser, S. Boucard, D. S. Covita, J. M. F. dos Santos, H. Fuhrmann, D. Gotta, A. Gruber, M. Hennebach, A. Hirtl, P. Indelicato, E.-O. Le Bigot, L. M. Simons, L. Stingelin, M. Trassinelli, J. F. C. A. Veloso, A. Wasser, and J. Zmeskal, Phys. Rev. A **88**, 022503 (2013).

[29] A. Gumberidze, M. Trassinelli, N. Adrouche, C. I. Szabo, P. Indelicato, F. Haranger, J. M. Isac, E. Lamour, E. O. Le Bigot, J. Merot *et al.*, Rev. Sci. Instrum. **81**, 033303 (2010).

[30] C. I. Szabo, P. Amaro, M. Guerra, S. Schlesser, A. Gumberidze, J. P. Santos, and P. Indelicato, in *Application of Accelerators in Research and Industry: Twenty-Second International Conference*, edited by F. D. McDaniel, B. L. Doyle, G. A. Glass, and Y. Wang, AIP Conf. Proc. 1525 (AIP, Melville, NY, 2013), pp. 68–72.

[31] M. Sanchez del Rio and R. J. Dejus, Proc. SPIE **5536**, 171 (2004).

[32] M. S. del Rio and R. J. Dejus, in *Synchrotron Radiation Instrumentation: Eighth International Conference*, edited by T. Warwick *et al.* (American Institute of Physics, 2004), pp. 784–787.

[33] M. S. del Río and R. J. Dejus, Proc. SPIE **8141**, 814115 (2011).

[34] J. Machado, G. Bian, N. Paul, M. Trassinelli, P. Amaro, M. Guerra, C. L. Szabo, A. Gumberidze, J. M. Isac, J. P. Santos,

J. P. Desclaux, and P. Indelicato, Phys. Rev. A **101**, 062505 (2020).

[35] M. Trassinelli, Proceedings **22**, 14 (2019).

[36] M. Trassinelli, Nucl. Instrum. Methods Phys. Res., Sect. B **408**, 301 (2017).

[37] C. Gordon and R. Trotta, Mon. Not. R. Astron. Soc. **382**, 1859 (2007).

[38] E. Tiesinga, P. J. Mohr, D. B. Newell, and B. N. Taylor, Rev. Mod. Phys. **93**, 025010 (2021).

[39] V. A. Yerokhin and K. Pachucki, Phys. Rev. A **81**, 022507 (2010).

[40] A. N. Artemyev, V. M. Shabaev, V. A. Yerokhin, G. Plunien, and G. Soff, Phys. Rev. A **71**, 062104 (2005).

[41] V. A. Yerokhin, V. Patkóš, and K. Pachucki, Phys. Rev. A **106**, 022815 (2022).

[42] G. W. Drake, Can. J. Phys. **66**, 586 (1988).

[43] J. E. Rice, M. L. Reinke, J. M. A. Ashbourn, C. Gao, M. M. Victora, M. A. Chilenski, L. Delgado-Aparicio, N. T. Howard, A. E. Hubbard, J. W. Hughes *et al.*, J. Phys. B **47**, 075701 (2014).

[44] J. E. Rice, M. A. Graf, J. L. Terry, E. S. Marmar, K. Giesing, and F. Bombarda, J. Phys. B **28**, 893 (1995).

[45] A. T. Payne, C. T. Chantler, M. N. Kinnane, J. D. Gillaspy, L. T. Hudson, L. F. Smale, A. Henins, J. A. Kimpton, and E. Takacs, J. Phys. B **47**, 185001 (2014).

[46] C. T. Chantler, D. Paterson, L. T. Hudson, F. G. Serpa, J. D. Gillaspy, and E. Takacs, Phys. Rev. A **62**, 042501 (2000).

[47] B. W. Batterman and H. Cole, Rev. Mod. Phys. **36**, 681 (1964).

[48] L. Kissel, B. Zhou, S. C. Roy, S. K. Sen Gupta, and R. H. Pratt, Acta Crystallogr., Sect. A **51**, 271 (1995).

[49] C. Chantler, J. Phys. Chem. Ref. Data **24**, 71 (1995).

[50] B. L. Henke, E. M. Gullikson, and J. C. Davis, At. Data Nucl. Data Tables **54**, 181 (1993).

[51] C. T. Chantler, J. Phys. Chem. Ref. Data **29**, 597 (2000).

[52] C. Q. Tran, C. T. Chantler, and Z. Barnea, Phys. Rev. Lett. **90**, 257401 (2003).

[53] E. Bergback Knudsen, A. Prodi, J. Baltser, M. Thomsen, P. Kjaer Willendrup, M. Sanchez del Rio, C. Ferrero, E. Farhi, K. Haldrup, A. Vickery *et al.*, J. Appl. Crystallogr. **46**, 679 (2013).

[54] L. Kissel, Radiat. Phys. Chem. **59**, 185 (2000).

[55] G. Hölzer, O. Wehrhan, and E. Förster, Cryst. Res. Technol. **33**, 555 (1998).

[56] S. Sasaki, KEK, Technical Report No. KEK–88-14, 1989 (unpublished).